

Multigap nodeless superconductivity in the Dirac intermetallic alloy V_2Ga_5 with one-dimensional vanadium chains

C. Q. Xu,^{1,*} C. C. Zhao,^{2,*} Y. Shen,^{3,*} D. Ratkovski,⁴ X. Ma,^{5,6} W. Zhou,⁷ Xunqing Yin,^{8,9,10} B. Li,¹¹ A. F. Bangura,⁴ Chao Cao,^{5,6} Baomin Wang,^{1,†} Ziming Zhu,^{3,‡} X. Ke,¹² Dong Qian,^{8,9,10} Shiyao Li,^{2,§} and Xiaofeng Xu^{13,||}

¹*School of Physical Science and Technology, Ningbo University, Ningbo 315211, China*

²*State Key Laboratory of Surface Physics, Department of Physics, Fudan University, Shanghai 200438, China*

³*Key Laboratory of Low-Dimensional Quantum Structures and Quantum Control of Ministry of Education, Department of Physics and Synergetic Innovation Center for Quantum Effects and Applications, Hunan Normal University, Changsha 410081, China*

⁴*National High Magnetic Field Laboratory, Tallahassee, Florida 32310, USA*

⁵*School of Physics, Zhejiang University, Hangzhou 310058, China*

⁶*Center for Correlated Matter, Zhejiang University, Hangzhou 310058, China*

⁷*School of Electronic and Information Engineering, Changshu Institute of Technology, Changshu 215500, China*

⁸*Key Laboratory of Artificial Structures and Quantum Control (Ministry of Education), School of Physics and Astronomy, Shanghai Jiao Tong University, Shanghai 200240, China*

⁹*Tsung-Dao Lee Institute, Shanghai Jiao Tong University, Shanghai 200240, China*

¹⁰*Collaborative Innovation Center of Advanced Microstructures, Nanjing 210093, China*

¹¹*Information Physics Research Center, Nanjing University of Posts and Telecommunications, Nanjing 210023, China*

¹²*Department of Physics and Astronomy, Michigan State University, East Lansing, Michigan 48824-2320, USA*

¹³*Department of Applied Physics, Zhejiang University of Technology, Hangzhou 310023, China*



(Received 7 November 2023; revised 16 January 2024; accepted 4 March 2024; published 21 March 2024)

Superconductors possessing diverse symmetry-enforced topological states have been a subject of intense interest as they are arguably one of the most feasible candidates to realize so-called topological superconductivity, a source of Majorana fermions that hold great promise for topological quantum computing. Here we study the low-lying quasiparticle excitations in the superconducting intermetallic alloy V_2Ga_5 by low-temperature heat capacity and ultra-low-temperature thermal conductivity measurements. It is found that its electronic specific heat can be fitted by either a d -wave gap or two s -wave gaps. However, the low- T thermal conductivity clearly points to the multiple nodeless energy gaps in its low-lying excitation spectrum. On the other hand, first-principles calculations reveal a multitude of topological fermions near the Fermi level, involving discrete Dirac nodes as well as Dirac nodal lines. These topological carriers, when condensed into Cooper pairs, provide a natural platform for achieving topologically nontrivial phases and possible Majorana fermions.

DOI: [10.1103/PhysRevB.109.L100506](https://doi.org/10.1103/PhysRevB.109.L100506)

Since the discovery of three-dimensional (3D) topological insulators (TIs) [1,2], the field of topological physics has witnessed a burgeoning development, with a vast landscape of emergent topological fermions and topological phenomena being revealed [3,4]. During this period, time-reversal-symmetric topological insulators, mirror Chern insulators, Dirac, Weyl, and nodal-line semimetals as well as higher-fold degenerate fermions and high-order TIs, etc. have all been predicted theoretically and discovered experimentally [5–12]. In addition, topological superconductors, whose inherent Majorana fermions can be braided and used in fault-tolerant quantum computation, have also sparked tremendous interest [13]. Although over 50% of all known materials, in the light of

theories of topological quantum chemistry [14], are supposed to host diverse symmetry-indicated nontrivial band topologies [15–18], only very few of them become superconductors at low temperatures and at ambient pressure [19–21]. This fact thus hinders the experimental detection of Majorana fermions and poses challenges for the application of them in topological quantum computing.

In the course of synthesizing the A -15-type superconductor V_3Ga [22], which shares the same crystal structure with the well-known Nb_3Sn alloy used in commercial superconducting magnets, another phase of vanadium-gallium alloy V_2Ga_5 was harvested unwittingly [23,24]. The V_2Ga_5 alloy crystallizes in the shape of long needles and shows type-II superconductivity below ~ 3.5 K. However, despite being first synthesized in the early 1960s, the superconducting properties of this quasi-one-dimensional V_2Ga_5 have been poorly investigated, let alone its topological properties.

Quasi-one-dimensional materials prove to be a fertile playground to study the emergent phenomena and emergent topological quasiparticles in condensed matter physics [25,26]. In

*These authors contributed equally to this work.

†wangbaomin@nbu.edu.cn

‡zimingzhu@hunnu.edu.cn

§shiyao_li@fudan.edu.cn

||xuxiaofeng@zjut.edu.cn

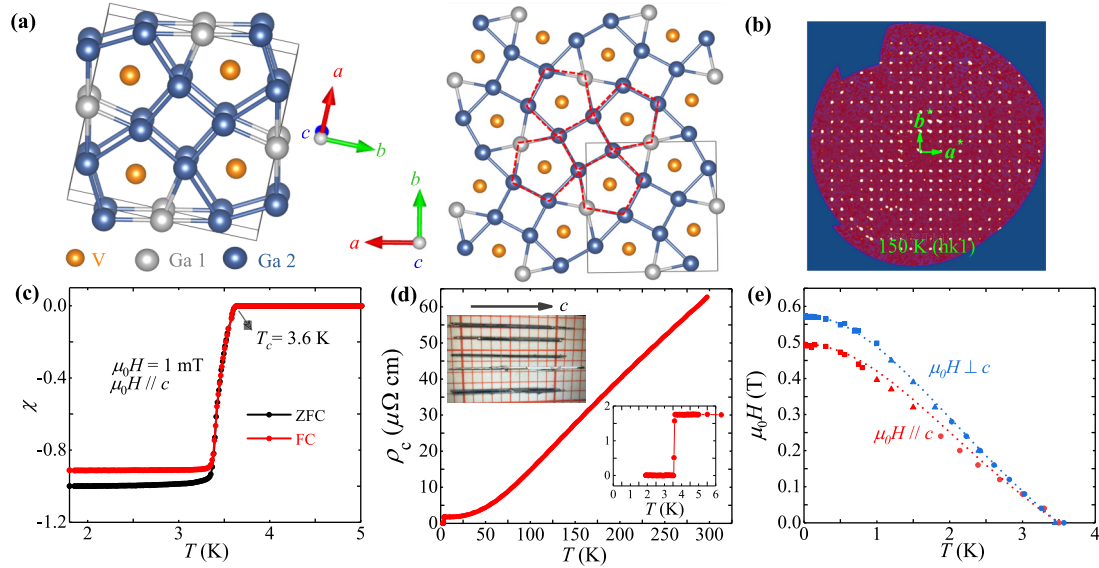


FIG. 1. (a) Schematic view of the crystal structure of V_2Ga_5 from two different perspectives. The solid box shows one unit cell and the Ga pentagons are highlighted in red. (b) The $(hk1)$ planes of reflections at 150 K in reciprocal space with unit vectors a^* and b^* marked. (c) Magnetic susceptibility as a function of temperature at a field of $\mu_0H = 1$ mT in ZFC and FC modes. (d) The temperature dependence of the intrachain resistivity ρ_c measured at zero field; the top inset is the image of as-grown crystals and the bottom inset is an expanded view of ρ_c at low temperatures. (e) The temperature dependence of the upper critical field μ_0H_{c2} and the fits to the GL theory along two directions. The circles, triangles, and squares are the data acquired from 4He , 3He cryostats, and dilution refrigerator, respectively.

this Letter, we report a detailed calorimetric and thermal transport study on single crystals of quasi-one-dimensional V_2Ga_5 with a superconducting critical temperature $T_c = 3.6$ K. While the electronic specific heat below T_c can be modeled by either a d -wave superconducting gap or two s -wave gaps, its ultra-low- T thermal conductivity unambiguously reveals multiple, nodeless gaps in its quasiparticle excitations. The first-principles calculations further corroborate the existence of topological carriers, including discrete Dirac nodes and the Dirac nodal lines in proximity to the Fermi level. Our study offers an intriguing material candidate for studying topological superconductivity at ambient pressure.

The experimental and computational methods used in this study as well as some supporting materials are given in the Supplemental Material (SM) [27] (see also references therein [23,24,28–34]). V_2Ga_5 crystallizes in the tetragonal space group $P4/mbm$ (No. 127). As illustrated in Fig. 1(a), its structure is comprised of alternating V and Ga sheets, and the Ga atoms reside in two Wyckoff positions, namely Ga 1 (Wyckoff position 2d) and Ga 2 (Wyckoff position 8m), in gray and blue colors, respectively. The ratio of Ga 1 to Ga 2 is 1:4. The Ga sheet consists of triangular, square, and pentagonal plaquettes and each Ga pentagon has one Ga 1 and four Ga 2; each Ga triangle has one Ga 1 and two Ga 2; the square has four Ga 2. Along the c axis, the V and Ga atoms form V-centered pentagonal channels; V is approximately at the center of the Ga pentagonal prism formed by ten Ga atoms (two Ga 1 and eight Ga 2). Hence, the basic structural motif is the V-centered pentagonal channels along the c axis. Since the density of states at the Fermi level is dominated by the V d -orbital [24], the conducting element is the one-dimensional vanadium chains along the c axis that are coupled to each other by the neighboring Ga ions. Considering the Ga atoms

also contribute to the density of states at the Fermi level [24], one would expect the V chains are rather strongly coupled in the transverse directions, reducing the overall anisotropy. In order to check the structure and the quality of V_2Ga_5 single crystals, we carried out the single-crystal x-ray diffraction measurement on a piece of as-grown crystal at 150 K and refined the data using SHELXT [35,36]. The lattice spots in reciprocal space are shown in Fig. 1(b); it is clearly seen that the primary Bragg diffractions in the a^*b^* plane have tetragonal patterns. The refinement yields the lattice parameters $a = b = 8.9820(3)$ Å, $c = 2.7005(2)$ Å [27], compared to $a = b = 8.936(3)$ Å, $c = 2.683(2)$ Å reported in Ref. [24].

Figure 1(c) shows the T -dependent magnetization curves in an applied field of 1 mT ($\mu_0H \parallel c$) under both zero-field-cooling (ZFC) and field-cooling (FC) protocols, after accounting for the demagnetization effect. Note that both magnetization curves exhibit large diamagnetic signals below $T_c \sim 3.6$ K, and the ZFC curve shows perfect diamagnetism of $\chi = -1$, suggesting 100% bulk superconductivity of V_2Ga_5 . The large FC diamagnetic signal is the manifestation of the weak vortex pinning force in this superconductor. Figure 1(d) depicts the zero-field intrachain ($I \parallel c$) resistivity, with the inset magnifying the low- T region. It is noteworthy that V_2Ga_5 shows T -linear metallic resistivity at high temperatures and it starts to bend over below ~ 70 K. Below $T_c \sim 3.6$ K, it undergoes a sharp superconducting transition, consistent with the magnetization measurement. Next, we map out the H_{c2} - T diagram in two field orientations ($\mu_0H \perp c$ and $\mu_0H \parallel c$), by sweeping temperature under fixed fields (in PPMS), as well as by field sweeping at constant temperatures (in the dilution refrigerator) [27]. As seen, the resultant μ_0H_{c2} - T diagram, determined by taking the midpoint where the resistivity drops to 50% of its normal-state value, is plotted in Fig. 1(e). The

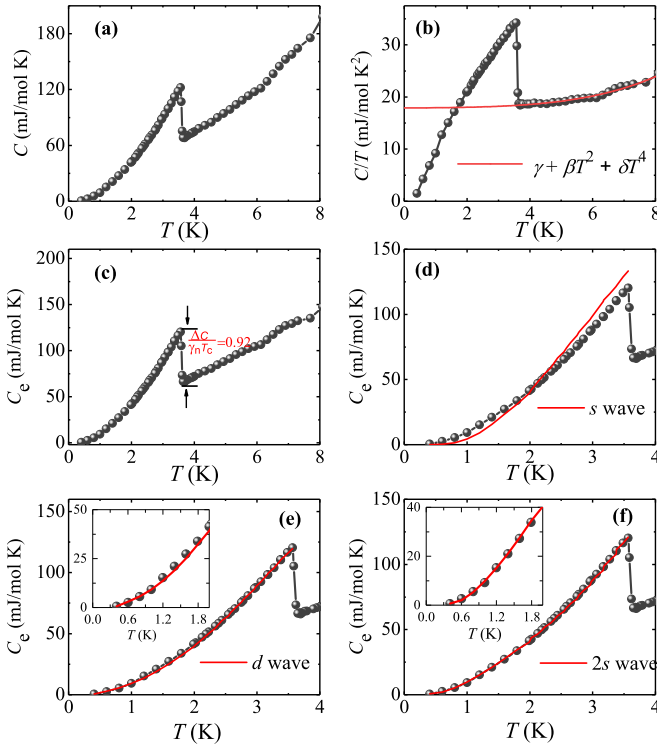


FIG. 2. (a) Zero-field heat capacity of V_2Ga_5 at low temperatures. (b) C/T as a function of T . The red line is the fit to $C/T = \gamma + \beta T^2 + \delta T^4$, with $\gamma = 17.92$ mJ/mol K^2 , $\beta = 2.40 \times 10^{-2}$ mJ/mol K^4 and $\delta = 1.09 \times 10^{-3}$ mJ/mol K^6 . (c) The electronic specific heat C_e after subtracting the phonon heat capacity. (d)–(f) The fits of C_e to the s -wave, d -wave, and two s -wave gaps, respectively. The insets of (e) and (f) zoom in on the low-temperature region.

$\mu_0 H_{c2}(T)$ in two field configurations can be well described by the Ginzburg-Landau (GL) formula $H_{c2}(T) = H_{c2}(0)(1 - t^2)/(1 + t^2)$, where t is the normalized temperature $t = T/T_c$. The $\mu_0 H_{c2}(0)$ is thus estimated to be 0.57 T for $\mu_0 H \perp c$, and 0.49 T for $\mu_0 H \parallel c$, both of which are much smaller than the Pauli limit $H_P \sim 1.84T_c$ (in this case, $H_P \sim 6.6$ Tesla) [37]. Moreover, it is surprising to note that $\mu_0 H_{c2}$ for $\mu_0 H \parallel c$ is even smaller than for $\mu_0 H \perp c$, contrary to most quasi-one-dimensional superconductors. According to anisotropic Ginzburg-Landau (GL) theory [38]:

$$\frac{H_{c2}^{\parallel c}}{H_{c2}^{\perp c}} = \frac{\xi^{\parallel c}}{\xi^{\perp c}} = \frac{\sqrt{\sigma^{\parallel c}}}{\sqrt{\sigma^{\perp c}}}, \quad (1)$$

where ξ is the coherence length and σ is the conductivity. For quasi-one-dimensional superconductors, due to the largest conductivity (the smallest resistivity) along the chain, H_{c2} is the largest with the field applied along the chain direction. For V_2Ga_5 , however, $H_{c2}^{\parallel c}$ is smaller than $H_{c2}^{\perp c}$. This immediately implies the interchain resistivity (ρ_{\perp}) may be even smaller than the intrachain one (ρ_c). This seems to be supported by the charge distribution calculations in Ref. [27]. Due to its needle-shaped morphology, however, it is difficult to measure the interchain resistivity (ρ_c) directly.

Figure 2 presents the detailed calorimetric study on the V_2Ga_5 single crystals. As depicted in Fig. 2(a), a clear heat capacity jump associated with the superconducting transition

is observed at 3.6 K, indicating the thermodynamic bulk transition. In order to isolate the electronic specific heat, the same data are plotted as C/T against temperature in Fig. 2(b). Subsequently, we fit the normal-state heat capacity by the formula $C/T = \gamma + \beta T^2 + \delta T^4$ above T_c and then extrapolated it to low temperatures, as illustrated by the red curve in Fig. 2(b). Note that the first γ term represents the electronic contribution, whereas the remaining two terms are phononic in origin.

By subtracting the phonon specific heat, the electronic heat capacity C_e is resolved in Fig. 2(c). In the superconducting state, C/T is approaching zero as $T \rightarrow 0$, indicating no significant impurity contributions and all carriers are condensed into Cooper pairs. This provides strong evidence for the high quality of the samples used. The heat capacity jump, quantified as $\Delta C/\gamma T_c$, equals 0.92, which is smaller than the weak-coupling s -wave BCS value of 1.43 but close to the d -wave value of 0.95 [39,40]. It is also noted that the low- T C_e deviates significantly from the exponential behaviors expected for the s -wave BCS gap, but rather is more consistent with the power-law dependence for a nodal superconducting gap. Next, we fit the C_e data using different gap functions. In the fitting, we employ the well-established α model, which assumes the temperature dependence of the energy gap $\Delta(T)$ is the same as the weak-coupling BCS behavior but its size is an adjustable parameter by $\Delta(T) = \alpha \Delta_{BCS}(T)$, where α is a constant [39,41,42]. α can be significantly larger than 1 for strongly coupled superconductors. Within this α model, the entropy S in the superconducting state is given by [39,43]:

$$S = -\frac{3\gamma_n}{k_B\pi^3} \int_0^{2\pi} \int_0^{\infty} [(1-f)\ln(1-f) + f\ln f] d\varepsilon d\phi, \quad (2)$$

where γ_n is the normal state γ , and f is the quasiparticle occupation number $f = (1 + e^{E/k_B T})^{-1}$ with $E = \sqrt{\varepsilon^2 + \Delta^2(\phi)}$ where $\Delta(\phi)$ is the angle dependence of the gap function. For an s -wave gap, this is angle independent and for a standard d -wave, $\Delta(T, \phi) = \Delta(T)\cos(2\phi)$. In the α model, we specify the temperature dependence of the gap function as $\Delta(\phi, T) = \alpha \Delta_{BCS}(\phi, T)$ [41]. Here $\Delta_{BCS}(\phi, T)$ is the weak coupling BCS gap function. Hence, $\Delta(\phi, T) = \Delta(T) = \alpha \Delta_{BCS}(T)$ for an s -wave gap and $\Delta(\phi, T) = \alpha \Delta_{BCS}(T)\cos(2\phi)$ for a d -wave gap. We refer the interested readers to Ref. [40] for more details. Therefore, the gap is assumed to take the BCS-like dependence on temperature but the magnitude is multiplied by a dimensionless parameter α , which depends on the strength of the electron-boson coupling. The specific heat is further calculated by $C_e = T(\partial S/\partial T)$.

In the single-gap fitting, only α is the free parameter and γ_n and T_c are determined from the experiment. The best fit to a single s -wave gap ($\alpha = 0.9$), as seen from Fig. 2(d), deviates significantly from the experimental data. In contrast, a d -wave gap ($\alpha = 0.99$) can fit the data very well, as demonstrated in Fig. 2(e) and its inset. We further fit the C_e data with two s -wave gaps. In this fitting, two sets of γ and α are assumed, each corresponding to one gap. The resultant fitting is displayed in Fig. 2(f). As seen, this two-gap fit can model the experimental data extremely well, indistinguishable from the d -wave fitting. All fitting parameters are listed in Table I for completeness.

TABLE I. The parameters derived from the fits to the specific heat data by using three different gap functions. γ_n is in the units of mJ/mol K^2 .

	T_c [K]	α		γ_n	
<i>s</i> -wave	3.6	0.9		17.92	
<i>d</i> -wave	3.6	0.99		17.92	
Two-gap	3.6	α_1	α_2	$\gamma_n^{(1)}$	$\gamma_n^{(2)}$
		1.32	0.54	4.91	13.01

Ultra-low-temperature thermal conductivity measurements provide more insights into the gap symmetry of V_2Ga_5 . Figure 3(a) displays the temperature dependence of the thermal conductivity in zero field in the millikelvin regime, plotted as κ/T versus $T^{2.47}$ so as to isolate the electronic term from the phonon contribution [44,45]. In low temperatures, for nonmagnetic materials, the thermal conductivity is comprised of two terms, $\kappa = \kappa_e + \kappa_{\text{ph}}$, denoting the contributions from electrons and phonons, respectively. Given that the electronic term is linear in T and the phonon term has a power-law dependence, the thermal conductivity is generally fitted to $\kappa/T = a + bT^{\alpha-1}$, where α is typically between 2 and 3, due to specular reflection of phonons at the sample boundary [44,45]. In this manner, the linear electronic contribution can be extracted by extrapolating κ/T to $T = 0$ K. This residual linear term κ_0/T contains a wealth of information on the gap symmetry of a superconductor. For an *s*-wave nodeless superconductor, for example, as the Fermi surface is fully gapped at low temperatures, no quasiparticles can be excited, therefore κ_0/T is essentially zero. By contrast, a sizable residual κ_0/T term is expected for a nodal superconductor, which has been observed in the overdoped *d*-wave cuprate superconductor $\text{Tl}_2\text{Ba}_2\text{CuO}_{6+\delta}$ (Tl-2201) [46] and some organic superconductors [47]. From Fig. 3(a), within the experimental uncertainty ($\pm 5 \mu\text{W K}^{-2}\text{cm}^{-1}$), no residual term κ_0/T is observed, providing compelling evidence for the nodeless superconductivity in V_2Ga_5 .

Another hint at the gap symmetry arises from the field dependence of the residual κ_0/T [48]. As shown in Fig. 3(b), we measured the low- T thermal conductivity at various fields. The residual κ_0/T at 0.5 T agrees well with the value expected from the Wiedemann-Franz law $\kappa_0/T = L_0/\rho_0$, where L_0 ($= 2.45 \times 10^8 \text{ W}\Omega\text{K}^2$) is the Lorenz ratio and ρ_0 is the residual resistivity at 0.5 T [$\rho_0(0.5 \text{ T}) = 2.69 \mu\Omega\text{cm}$ for this sample]. The verification of the Wiedemann-Franz law in the normal state corroborates the reliability of our thermal conductivity measurements. The field dependence of κ_0/T of V_2Ga_5 , together with those from some other well-studied superconductors, when normalized to their respective normal-state values and plotted against H/H_{c2} , is encapsulated in Fig. 3(c). In this plot, similar data for the clean *s*-wave superconductor Nb [49], the dirty *s*-wave superconducting alloy InBi [50], the multiband *s*-wave superconductor NbSe₂ [51], as well as the overdoped *d*-wave cuprate superconductor Tl-2201 [46], are all incorporated as a comparison.

For single-band clean *s*-wave superconductors, such as the elemental Nb superconductor [49], due to the energy gap over

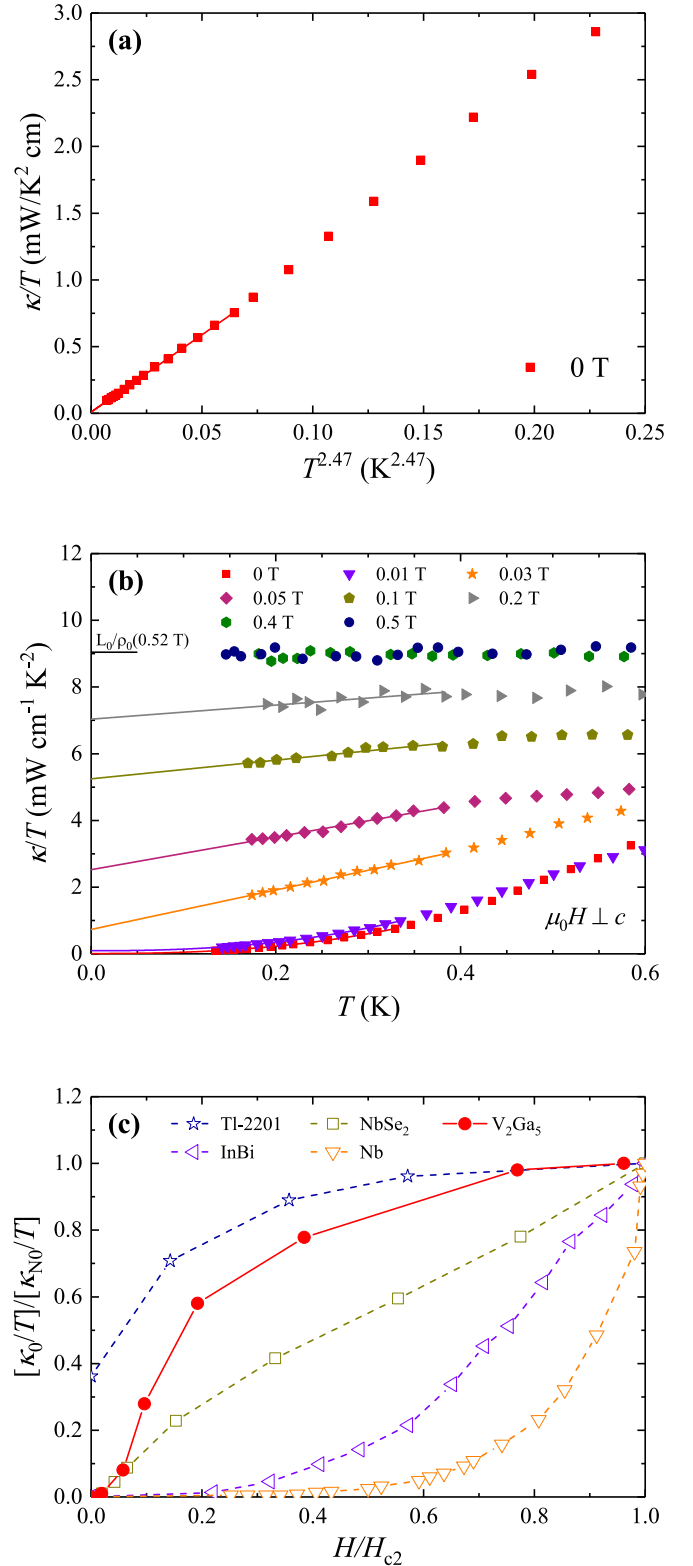


FIG. 3. (a) The temperature dependence of thermal conductivity κ in zero field, plotted as κ/T versus $T^{2.47}$, gives a negligible residual term κ_0/T . (b) Low- T thermal conductivity at various fields ($\mu_0 H \perp c$). L_0/ρ indicates the value expected from the Wiedemann-Franz law $\kappa/T = L_0/\rho$. (c) Normalized residual linear term κ_0/T of V_2Ga_5 as a function of H/H_{c2} , with similar data for other superconductors included for comparison.

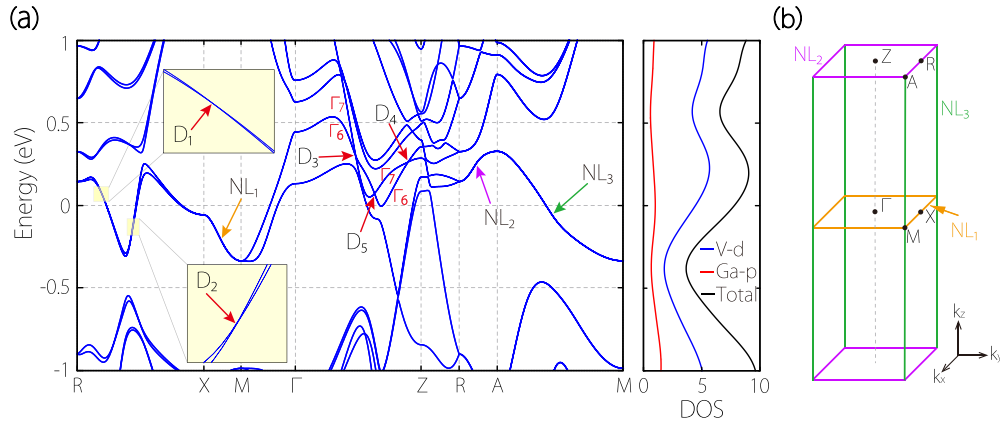


FIG. 4. (a) Calculated band structure along the high-symmetry paths along with DOS for V_2Ga_5 in the presence of SOC. (b) shows the distributions of the three nodal lines, i.e., NL_1 , NL_2 , and NL_3 , in the entire BZ, which connect together at A and M and form a nodal network. Here time-reversal-invariant momenta are marked by the black points.

the full Fermi surface, quasiparticles are difficult to excite and are generally localized within the vortex core [48], leading to a slow exponential growth of κ_0/T versus H . Likewise, for dirty s -wave superconductors (e.g., InBi), κ_0/T exhibits an exponential H dependence at low fields, and grows linearly when the field is approaching H_{c2} [50]. For the nodal superconductor TI-2201, on the contrary, apart from the substantial residual κ_0/T at zero field, a small field can induce a rapid growth of quasiparticle excitations due to the Volovik effect, thus the low-field κ_0/T displays a \sqrt{H} dependence [46]. In the case of multigap nodeless superconductors, however, the magnetic field dependence of κ_0/T lies between these two extremes and its profile relies on the ratio between the large and small gaps, as seen for the prototypical two-band superconductor NbSe₂ where the ratio of different gap magnitudes is approximately 3 [51]. A rapid rise in low fields can thus be attributed to the fast suppression of the smaller gap by the applied field. The field profile for V_2Ga_5 supports this picture and can likewise be classified as a multigap nodeless superconductor.

Figure 4(a) illustrates the calculated band structure of V_2Ga_5 along the high-symmetry paths, with spin-orbit coupling (SOC) included, as well as the projected density of states (PDOS). It should be mentioned that the main symmetries in V_2Ga_5 compound have inversion symmetry (\mathcal{P}), time-reversal symmetry (\mathcal{T}), a fourfold rotation along the z axis (C_{4z}), a twofold rotation along the z axis (C_{2z}), a twofold screw rotation along the x axis $\tilde{C}_{2x} = \{C_{2x} | \frac{1}{2} \frac{1}{2} 0\}$, a horizontal mirror symmetry M_z , and two vertical glide mirror symmetries $\tilde{M}_x = \{M_x | \frac{1}{2} \frac{1}{2} 0\}$ and $\tilde{M}_y = \{M_y | \frac{1}{2} \frac{1}{2} 0\}$ (here x, y , and z refer to the a, b, c axes, respectively). From the PDOS, it is clear that the low-energy bands are mainly contributed by V- d and Ga- p orbitals. One can observe that several bands cross each other around the Fermi level, leading to the formation of Dirac nodes and nodal lines in the whole BZ. After careful inspection, we find there exist two types of Dirac points along Γ -Z and R-X, with $D_1 \sim D_4$ being type-II dispersion and D_5 being type-I dispersion. Furthermore, the crossed bands along Γ -Z host Γ_6 and Γ_7 of the double irreducible representations, indicating that Dirac points on this path ($D_3 \sim D_5$) are protected by the combined \mathcal{PT} , C_{4z} , and \tilde{M}_y [52,53]. In addition,

the Dirac points D_1 and D_2 along R-X are guaranteed by the combined \mathcal{PT} , \tilde{M}_y , and C_{2z} [54,55]. On the other hand, two doubly degenerate bands due to \mathcal{P} and \mathcal{T} will stick together along the XM, RA, and AM directions, leading to the appearance of a nodal network as depicted in Fig. 4(b). Here NL_1 , NL_2 are protected by the combined \mathcal{PT} , M_z and \tilde{C}_{2x} , and NL_3 are protected by the combined \mathcal{PT} , C_{4z} , and \tilde{M}_x [54,55].

Having revealed a wealth of topological carriers in the title material, we remark on the implication of these findings for the possible topological superconductivity. Its topology, according to the calculations, is very robust against correlation effects of V-3d electrons, that is, tuning the Coulomb U values from 1–5 eV does not change significantly the main topological features [27]. Moreover, the topological fermions are predominantly located in the vicinity of Fermi level. Upon entering the superconducting state, it is these fermions that are eventually condensed into Cooper pairs. The robustness of topological features, as well as the proximity to the Fermi level, is important for both topological superconductivity and technical applications.

To summarize, we have successfully synthesized the intermetallic alloy V_2Ga_5 with the one-dimensional needle-like morphology. This alloy is characterized by the one-dimensional vanadium chains in structure and a superconducting transition temperature of $T_c \sim 3.6$ K. Based on the calorimetric and thermal conductivity measurements, its superconducting low-lying quasiparticle excitations are found to be more compatible with a multigap nodeless superconducting ground state. Importantly, the band structure of this compound hosts a cornucopia of topological Dirac nodes and Dirac nodal lines near the Fermi level. Coupled with its superconducting ground state, these observations place V_2Ga_5 as an interesting material candidate for exploring topological superconductivity in this class of materials. As a future direction, it is desirable to probe the putative Majorana fermions in this system by the point contact spectroscopy and/or the scanning tunneling microscopy/spectroscopy directly.

We thank Zhu'An Xu, Jinguang Cheng, Toni Shiroka, Caroline Andrew, Michael Smidman, and Jinke Bao for

helpful discussions. This work was sponsored by Zhejiang Provincial Natural Science Foundation of China (Grant No. LD24F040001) and National Natural Science Foundation of China (Grants No. 12274369, No. 11974061, No. 12304071,

No. 12174064, and No. 11704117). Z.Z. was supported by the Project of Educational Commission of Hunan Province of China (Grant No. 21A0066), the Hunan Provincial Natural Science Foundation of China (Grant No. 2022JJ30370).

- [1] M. Z. Hasan and C. L. Kane, Colloquium: Topological insulators, *Rev. Mod. Phys.* **82**, 3045 (2010).
- [2] X.-L. Qi and S.-C. Zhang, Topological insulators and superconductors, *Rev. Mod. Phys.* **83**, 1057 (2011).
- [3] Z. Wang, A. Alexandradinata, R. J. Cava, and B. A. Bernevig, Hourglass fermions, *Nature (London)* **532**, 189 (2016).
- [4] B. J. Wieder, B. Bradlyn, Z. Wang, J. Cano, Y. Kim, H.-S. D. Kim, A. M. Rappe, C. L. Kane, and B. A. Bernevig, Wallpaper fermions and the nonsymmorphic Dirac insulator, *Science* **361**, 246 (2018).
- [5] N. P. Armitage, E. J. Mele, and A. Vishwanath, Weyl and Dirac semimetals in three-dimensional solids, *Rev. Mod. Phys.* **90**, 015001 (2018).
- [6] B. Q. Lv, T. Qian, and H. Ding, Experimental perspective on three-dimensional topological semimetals, *Rev. Mod. Phys.* **93**, 025002 (2021).
- [7] T. H. Hsieh, H. Lin, J. Liu, W. Duan, A. Bansil, and L. Fu, Topological crystalline insulators in the SnTe material class, *Nature Commun.* **3**, 982 (2012).
- [8] B. Bradlyn, J. Cano, Z. Wang, M. G. Vergniory, C. Felser, R. J. Cava, and B. A. Bernevig, Beyond Dirac and Weyl fermions: Unconventional quasiparticles in conventional crystals, *Science* **353**, aaf5037 (2016).
- [9] B. Q. Lv, Z.-L. Feng, Q.-N. Xu, X. Gao, J.-Z. Ma, L.-Y. Kong, P. Richard, Y.-B. Huang, V. N. Strocov, C. Fang, H.-M. Weng, Y.-G. Shi, T. Qian, and H. Ding, Observation of three-component fermions in the topological semimetal molybdenum phosphide, *Nature (London)* **546**, 627 (2017).
- [10] C. Yue, Y. Xu, Z. Song, H. Weng, Y.-M. Lu, C. Fang, and X. Dai, Symmetry-enforced chiral hinge states and surface quantum anomalous Hall effect in the magnetic axion insulator $\text{Bi}_{2-x}\text{Sm}_x\text{Se}_3$, *Nature Phys.* **15**, 577 (2019).
- [11] A. Tiwari, M.-H. Li, B. A. Bernevig, T. Neupert, and S. A. Parameswaran, Unhinging the surfaces of higher-order topological insulators and superconductors, *Phys. Rev. Lett.* **124**, 046801 (2020).
- [12] C. Chen, X.-T. Zeng, Z. Chen, Y. X. Zhao, X.-L. Sheng, and S. A. Yang, Second-order real nodal-line semimetal in three-dimensional graphdiyne, *Phys. Rev. Lett.* **128**, 026405 (2022).
- [13] C. Nayak, S. H. Simon, A. Stern, M. Freedman, and S. D. Sarma, Non-Abelian anyons and topological quantum computation, *Rev. Mod. Phys.* **80**, 1083 (2008).
- [14] B. Bradlyn, L. Elcoro, J. Cano, M. G. Vergniory, Z. Wang, C. Felser, M. I. Aroyo, and B. A. Bernevig, Topological quantum chemistry, *Nature (London)* **547**, 298 (2017).
- [15] T. Zhang, Y. Jiang, Z. Song, H. Huang, Y. He, Z. Fang, H. Weng, and C. Fang, Catalogue of topological electronic materials, *Nature (London)* **566**, 475 (2019).
- [16] M. G. Vergniory, L. Elcoro, C. Felser, N. Regnault, B. A. Bernevig, and Z. Wang, A complete catalogue of high-quality topological materials, *Nature (London)* **566**, 480 (2019).
- [17] F. Tang, H. C. Po, A. Vishwanath, and X. Wan, Comprehensive search for topological materials using symmetry indicators, *Nature (London)* **566**, 486 (2019).
- [18] M. G. Vergniory, B. J. Wieder, L. Elcoro, S. S. P. Parkin, C. Felser, B. A. Bernevig, and N. Regnault, All topological bands of all nonmagnetic stoichiometric materials, *Science* **376**, eabg9094 (2022).
- [19] L. Fu and E. Berg, Odd-parity topological superconductors: Theory and application to $\text{Cu}_x\text{Bi}_2\text{Se}_3$, *Phys. Rev. Lett.* **105**, 097001 (2010).
- [20] Y. Ando and L. Fu, Topological crystalline insulators and topological superconductors: From concepts to materials, *Annu. Rev. Condens. Matter Phys.* **6**, 361 (2015).
- [21] M. Sato and Y. Ando, Topological superconductors: A review, *Rep. Prog. Phys.* **80**, 076501 (2017).
- [22] J. H. N. V. Vucht, H. Bruning, and H. C. Donkersloot, New compounds related to the superconductors V_3Ga and Nb_3Sn , *Phys. Lett.* **7**, 297 (1963).
- [23] W. J. Kitchingman and P. L. Norman, X-ray diffraction studies of the ternary alloys $(\text{V,Mn})_2\text{Ga}_5$, *Acta Cryst. B* **28**, 1311 (1972).
- [24] K. C. Lohring, C. E. Check, J. Zhang, S. Li, C. Zheng, and K. Rogacki, Single crystal growth, bonding analysis and superconductivity of V_2Ga_5 , *J. Alloy. Compd.* **347**, 72 (2002).
- [25] P. Chudzinski, M. Berben, X. Xu, N. Wakeham, B. Bernáth, C. Duffy, R. D. H. Hinlopen, Y.-T. Hsu, S. Wiedmann, P. Tinnemans, R. Jin, M. Greenblatt, and N. E. Hussey, Emergent symmetry in a low-dimensional superconductor on the edge of Mottness, *Science* **382**, 792 (2023).
- [26] C. Xu, Y. Liu, P. Cai, B. Li, W. Jiao, Y. Li, J. Zhang, W. Zhou, B. Qian, X. Jiang, Z. Shi, R. Sankar, J. Zhang, F. Yang, Z. Zhu, P. Biswas, D. Qian, X. Ke, and X. Xu, Anisotropic transport and quantum oscillations in the quasi-one-dimensional TaNiTe_5 : Evidence for the nontrivial band topology, *J. Phys. Chem. Lett.* **11**, 7782 (2020).
- [27] See Supplemental Material at <http://link.aps.org/supplemental/10.1103/PhysRevB.109.L100506> for more information on the experimental setups, computational method and the additional data.
- [28] Y. Liu, C.-Q. Xu, W.-H. Jiao, P.-G. Cai, B. Li, W. Zhou, B. Qian, X.-F. Jiang, R. Kalaivaman, R. Sankar, X.-L. Ke, G.-H. Cao, and X. Xu, Anisotropic transport in a possible quasi-one-dimensional topological candidate: TaNi_2Te_3 , *Tungsten* **5**, 325 (2023).
- [29] X. B. Shi, P. He, and W. W. Zhao, Dual topology in van der Waals-type superconductor $\text{Nb}_2\text{S}_2\text{C}$, *Tungsten* **5**, 357 (2023).
- [30] P. E. Blöchl, Projector augmented-wave method, *Phys. Rev. B* **50**, 17953 (1994).
- [31] G. Kresse and J. Furthmüller, Efficient iterative schemes for *ab initio* total-energy calculations using a plane-wave basis set, *Phys. Rev. B* **54**, 11169 (1996).

- [32] G. Kresse and D. Joubert, From ultrasoft pseudopotentials to the projector augmented-wave method, *Phys. Rev. B* **59**, 1758 (1999).
- [33] J. P. Perdew, K. Burke, and M. Ernzerhof, Generalized gradient approximation made simple, *Phys. Rev. Lett.* **77**, 3865 (1996).
- [34] S. L. Dudarev, G. A. Botton, S. Y. Savrasov, C. J. Humphreys, and A. P. Sutton, Electron-energy-loss spectra and the structural stability of nickel oxide: An LSDA+U study, *Phys. Rev. B* **57**, 1505 (1998).
- [35] G. M. Sheldrick, SHELXT - Integrated space-group and crystal-structure determination, *Acta Cryst. A* **71**, 3 (2015).
- [36] O. V. Dolomanov, L. J. Bourhis, R. J. Gildea, J. A. K. Howard, and H. Puschmann, *OLEX2*: a complete structure solution, refinement and analysis program, *J. Appl. Cryst.* **42**, 339 (2009).
- [37] F. Zuo, J. S. Brooks, R. H. McKenzie, J. A. Schlueter, and J. M. Williams, Paramagnetic limiting of the upper critical field of the layered organic superconductor κ -(BEDT-TTF)₂Cu(SCN)₂, *Phys. Rev. B* **61**, 750 (2000).
- [38] J. F. Mercure, A. F. Bangura, X. Xu, N. Wakeham, A. Carrington, P. Walmsley, M. Greenblatt, and N. E. Hussey, Upper critical magnetic field far above the paramagnetic pair-breaking limit of superconducting one-dimensional Li_{0.9}Mo₆O₁₇ single crystals, *Phys. Rev. Lett.* **108**, 187003 (2012).
- [39] O. J. Taylor, A. Carrington, and J. A. Schlueter, Specific-heat measurements of the gap structure of the organic superconductors κ -(ET)₂Cu[N(CN)₂]Br and κ -(ET)₂Cu(NCS)₂, *Phys. Rev. Lett.* **99**, 057001 (2007).
- [40] O. Taylor, Specific heat studies of the organic superconductors κ -(BEDT-TTF)₂Cu[N(CN)₂]Br and κ -(BEDT-TTF)₂Cu(NCS)₂, Ph.D. thesis, Univeristy of Bristol, 2007.
- [41] H. Padamsee, J. E. Neighbor, and C. A. Shiffman, Quasiparticle phenomenology for thermodynamics of strong-coupling superconductors, *J. Low Temp. Phys.* **12**, 387 (1973).
- [42] P. Popovich, A. Boris, O. Dolgov, A. A. Golubov, D. L. Sun, C. T. Lin, R. K. Kremer, and B. Keimer, Specific heat measurements of Ba_{0.68}K_{0.32}Fe₂As₂ single crystals: Evidence for a multiband strong-coupling superconducting state, *Phys. Rev. Lett.* **105**, 027003 (2010).
- [43] X. Xu, B. Chen, W. H. Jiao, B. Chen, C. Q. Niu, Y. K. Li, J. H. Yang, A. F. Bangura, Q. L. Ye, C. Cao, J. H. Dai, G. Cao, and N. E. Hussey, Evidence for two energy gaps and Fermi liquid behavior in the SrPt₂As₂ superconductor, *Phys. Rev. B* **87**, 224507 (2013).
- [44] S. Y. Li, J.-B. Bonnemaïson, A. Payeur, P. Fournier, C. H. Wang, X. H. Chen, and L. Taillefer, Low-temperature phonon thermal conductivity of single-crystalline Nd₂CuO₄: Effects of sample size and surface roughness, *Phys. Rev. B* **77**, 134501 (2008).
- [45] M. Sutherland, D. G. Hawthorn, R. W. Hill, F. Ronning, S. Wakimoto, H. Zhang, C. Proust, E. Boaknin, C. Lupien, L. Taillefer, R. Liang, D. A. Bonn, W. N. Hardy, R. Gagnon, N. E. Hussey, T. Kimura, M. Nohara, and H. Takagi, Thermal conductivity across the phase diagram of cuprates: Low-energy quasiparticles and doping dependence of the superconducting gap, *Phys. Rev. B* **67**, 174520 (2003).
- [46] C. Proust, E. Boaknin, R. W. Hill, L. Taillefer, and A. P. Mackenzie, Heat transport in a strongly overdoped cuprate: Fermi liquid and a pure *d*-wave BCS superconductor, *Phys. Rev. Lett.* **89**, 147003 (2002).
- [47] S. Belin, K. Behnia, and A. Deluzet, Heat conduction in κ -(BEDT-TTF)₂Cu(NCS)₂, *Phys. Rev. Lett.* **81**, 4728 (1998).
- [48] H. Shakeripour, C. Petrovic, and L. Taillefer, Heat transport as a probe of superconducting gap structure, *New J. Phys.* **11**, 055065 (2009).
- [49] J. Lowell and J. B. Sousa, Mixed-state thermal conductivity of type II superconductors, *J. Low Temp. Phys.* **3**, 65 (1970).
- [50] J. O. Willis and D. M. Ginsberg, Thermal conductivity of superconducting alloy films in a perpendicular magnetic field, *Phys. Rev. B* **14**, 1916 (1976).
- [51] E. Boaknin, M. A. Tanatar, J. Paglione, D. Hawthorn, F. Ronning, R. W. Hill, M. Sutherland, L. Taillefer, J. Sonier, S. M. Hayden, and J. W. Brill, Heat conduction in the vortex state of NbSe₂: Evidence for multiband superconductivity, *Phys. Rev. Lett.* **90**, 117003 (2003).
- [52] B.-J. Yang and N. Nagaosa, Classification of stable three-dimensional Dirac semimetals with nontrivial topology, *Nature Commun.* **5**, 4898 (2014).
- [53] Z. Wang, H. Weng, Q. Wu, X. Dai, and Z. Fang, Three-dimensional Dirac semimetal and quantum transport in Cd₃As₂, *Phys. Rev. B* **88**, 125427 (2013).
- [54] Z.-M. Yu, Z. Zhang, G.-B. Liu, W. Wu, X.-P. Li, R.-W. Zhang, S. A. Yang, and Y. Yao, Encyclopedia of emergent particles in three-dimensional crystals, *Sci. Bull.* **67**, 375 (2022).
- [55] F. Tang and X. Wan, Complete classification of band nodal structures and massless excitations, *Phys. Rev. B* **105**, 155156 (2022).